Zwitterionic Janus Dendrimer with Distinct Functional Disparity for Enhanced Protein Delivery

Lili Wang[†], **Changying Shi**[†], **Xu Wang**[†,¶], **Dandan Guo**[†], **Thomas M. Duncan**[‡], and **Juntao Luo**[†,§,#]

[†]Department of Pharmacology, State University of New York Upstate Medical University, Syracuse, New York 13210, United States

[¶]National Engineering Research Center for Colloidal Materials, School of Chemistry and Chemical Engineering, Shandong University, Jinan 250100, PR China.

[‡]Department of Biochemistry and Molecular Biology, State University of New York Upstate Medical University, Syracuse, New York 13210, United States

[§]Department of Surgery, State University of New York Upstate Medical University, Syracuse, New York 13210, United States

[#]Upstate Cancer Center, State University of New York Upstate Medical University, Syracuse, New York 13210, United States
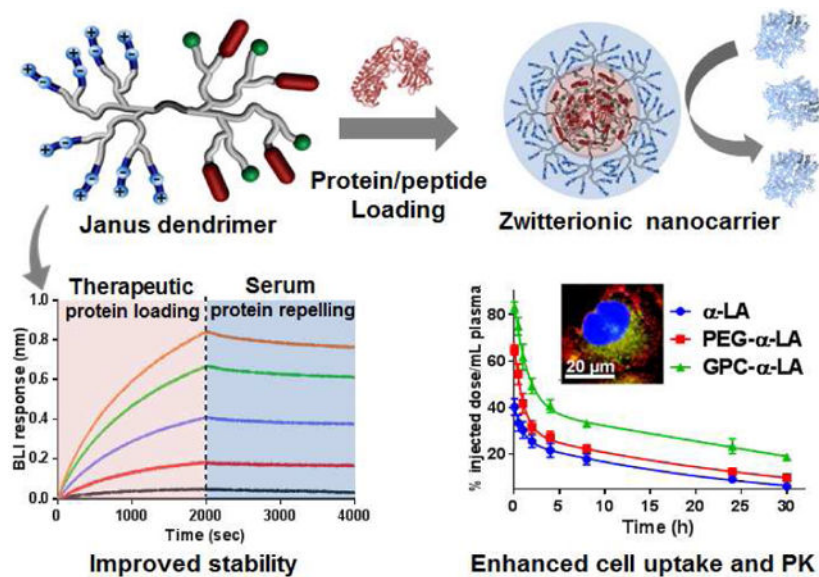
Abstract

The development of a facile protein delivery vehicle is challenging and remains an unmet demand for clinical applications. The well-defined structure and functionality of a nanocarrier are highly desirable for the reproducibility and regulatory compliance. Herein, we report for the first time a novel Janus dendrimer (JD) system, comprised of two distinct dendrons with superior protein binding and protein repelling properties, respectively, for efficient spontaneous protein loading and enhanced *in vivo* protein delivery. Core-forming dendron is tethered with a combination of charged and hydrophobic moieties, which coat protein surface efficiently via the multivalent and synergistic interactions. Zwitterionic peripheries on the counter dendron endow the nanoparticle (<20 nm) with a highly hydrophilic and antifouling surface, which efficiently prevents serum protein adsorption and exchange as demonstrated in biolayer interferometry assay, therefore, reducing premature protein release. Surprisingly, JD nanocarriers containing biomimicking glycerylphosphorylcholine (GPC) surface significantly enhanced the intracellular uptake of protein therapeutics specifically in cancer cells, compared with zwitterionic carboxybetain (CB)-JD and PEGylated nanocarriers. The zwitterionic JD nanocarriers greatly prolonged the *in vivo* pharmacokinetic profiles of payloads relative to the PEGylated nanocarriers. Janus nanocarrier controlled the *in vivo* release of insulin and improved the blood sugar control in mice.

Graphical Abstract

INTRODUCTION

The encapsulation and delivery of protein therapeutics is challenging due to the hydrophilic and vulnerable protein structures.[1] Charged lipids, polymers and dendrimers have been applied to form nanocomplexes for intracellular protein delivery.[2-10] Similar to the conventional transfection reagents, these charged material-protein nanocomplexes generally aggregate into large particles with unfavorable surface charges and chemistries, causing fast immune clearance and nonspecific cell uptakes of nanoparticles, therefore, preventing their systemic application for *in vivo* protein delivery. To address this issue, we have previously developed linear-dendritic telodendrimer (TD) nanoplatform for *in situ* protein coating and *in vivo* protein delivery.[11, 12] Multiple charged and hydrophobic moieties are precisely decorated on the peripheries of the dendritic oligolysine, which was tethered at the focal point with a linear PEG chain. Such flexible scaffold binds protein surfaces efficiently via the multivalent and synergistic combination of electrostatic and hydrophobic interactions. [11, 12]

The interaction of nanoparticle with the biological system is crucial for the *in vivo* fate of nanotherapeutics.[13, 14] Surface chemistry of nanoparticle largely determines the protein corona formation, which marks nanoparticles with biological identity, therefore, determining their *in vivo* fate and biodistribution.[15] Polyethylene glycol (PEG) is the most commonly used surface chemistry on nanotherapeutics, including our TD system. The packing density and molecular weight of the flexible PEG chains may affect the protein adsorption on the nanoparticle in plasma.[16] In addition, the amphiphilic nature of PEG may also contribute

to the intrinsic protein interactions,[17-19] which may lead to the immune cell clearance of nanoparticles.[20, 21] For protein delivery, the formation of serum protein corona may further induce protein exchange and premature release of therapeutic protein, which poses additional delivery challenges and needs to be minimized. Zwitterionic polymers have been explored as antifouling surface chemistries for biomedical applications, majorly attributed to the exceptional hydrophilicity and biocompatibility.[22-24] However, it is known that zwitterionic polymers have limited solubilities in organic solvents and poor dissolution even in some aqueous solutions, due to the overwhelming network formation by the intermolecular charge relay.[25] It may limit the chemical synthesis, modification and application of nanoparticles composed of zwitterionic block-copolymers. Alternatively, we rationally designed a zwitterionic dendritic crown to replace linear PEG in TD, yielding a Janus dendrimer to enhance protein delivery. The clustered zwitterionic moieties on the dendritic periphery not only provide more efficient sheltering effects than linear polymers, but also minimize the incidence of intermolecular charge relay, thus, dissolving readily in polar solvents and remitting the nanocarrier synthesis.

Amphiphilic Janus dendrimers (JD) have been constructed generally to fuse hydrophobic dendron with the hydrophilic or charged dendrons with spatial segregation, which self-assemble into dendrimersomes,[26, 27] nanoparticles[28] or hydrogels[29] potentially for drug or gene delivery. To the best of our knowledge, this is the first time to report zwitterionic JD by integrating two dendrons rationally with the distinct functions for protein repelling and protein binding, respectively. The well-defined JD structure is highly demanded for the clinical development of nanotherapeutics in favor of quality control and reproducibility. In addition, the freely engineerable chemical structures of JD allow to fine-tune protein binding and release profiles to optimize the *in vivo* efficacy of protein nanotherapeutics. The optimized JD with phosphorylcholine surface chemistry significantly improved *in vitro* and *in vivo* stability, prolonged blood circulation, increased cancer cell uptake, and enhanced *in vivo* insulin delivery for blood sugar control.

RESULTS AND DISCUSSION

Synthesis of Zwitterionic Janus Dendrimers.

The zwitterionic Janus dendrimers (JD) were constructed through a combination of solid-phase and liquid-phase peptide chemistry approaches. The stepwise peptide synthesis using orthogonally protected amino acids allows for the sequential introduction of unique protein binding moieties[11, 30] and antifouling zwitterionic components on the spatially segregated dendrons in the constructed dendrimers. Two types of zwitterionic surfaces were exploited to optimize protein repelling and biocompatibility properties of JDs. The unique zwitterionic JDs were designed precisely to integrate the seemly opposite domains for protein binding and protein repelling in one nanocarrier, allowing for coating protein *in situ* into nanoparticles and displaying the antifouling moieties on the surfaces of nanoparticles (Figure 1a).

Solid-phase peptide chemistry was utilized to construct dendrons with zwitterionic peripheries on an oligolysine scaffold via a divergent approach. A stepwise synthetic pathway is illustrated in Figure S1. Onto a cleavable Rink amide resin, protected lysine

(Fmoc-Lys(Boc)-OH) was initially conjugated, and Boc-protecting group remained to preserve the reactive amine group for the counter dendron synthesis. Subsequently, Fmoc-Lys(Fmoc)-OH served as branching unit for the iterative oligolysine dendron synthesis via Fmoc-peptide chemistry. Carboxybetain (CB) and glycerylphosphorylcholine (GPC) were selected as zwitterionic moieties for the precise dendron functionalization through reactions with the peripheral amine groups. zwitterionic CB was introduced via a nucleophilic reaction of bromoacetic acid with a tertiary amine introduced on the periphery of oligolysine to yield carboxylate and quaternary ammonium zwitterionic charge pairs (Figure S1a).[31] The primary hydroxyl group of GPC was converted to carboxylic acid by reacting with succinic anhydride, which was then attached to the peripheries of oligolysine dendrons (Figure S1b **and** S2). MALDI-TOF MS spectra unambiguously characterized the structural integrity of the intermediates cleaved from the resin (Figure 1b). The explicit presence of molecular ion peaks was detected for all intermediates by MALDI-TOF MS (Figure S3), highlighting the precise synthesis of dendrons as designed and ensuring the reproducible properties observed in the following studies. The zwitterionic dendrons were cleaved efficiently from the solid resin and denoted as $D\text{-}CB_n\text{-}NH_2$ and $D\text{-}GPC_n\text{-}NH_2$, respectively, (where n indicates the number of peripheral functional groups). The dendrons with multiple zwitterionic moieties possessing charge pairs are hardly desorbed and detected in MALDI-TOF analysis. Instead, the chemical integrity of the precursor dendron with tertiary amines ($D\text{-}DMBA_{16}\text{-}NH_2$) was evidenced by the sole and precise molecular ion peak at 4130.894 Dalton ($[M+Na]^+$, m/z) (Figure 1b), and the proportional peak integrations were detected in ^1H NMR analysis (Figure S4). The chemical compositions of zwitterionic dendrons were also elucidated by ^1H NMR analysis (Figure S5). Unlike linear zwitterionic polymers suffering from poor solubility in organic solvents,[32, 33] zwitterionic dendrons are readily soluble in water and both polar protic and aprotic organic solvents, e.g. Methanol, DMF, DMSO, which facilitates the further JD synthesis and therapeutic loading. The zwitterionic groups in dendritic architectures are inclined to reduce intermolecular interactions by the favored intramolecular zwitterionic charge relays, which may provide better surface shielding effects and better solubility than the linear polymers.

A reactive primary amine at the focal point of the zwitterionic dendron was deprotected to initiate the counter dendron synthesis via solution-phase peptide chemistry following our previous procedure.[11, 34] The second dendron was decorated with the positively-charged arginine (Arg) and heptadecanoic acid (C17) at the N-terminal peripheries, which were demonstrated to have synergy in protein binding in our previous studies.[11, 34] The guanidinium groups in Arginine interact with protein payload through electrostatic force, which can be enhanced by the reduced polarity caused by the adjacent hydrophobic groups. The aliphatic C17 is a flexible hydrophobic moiety, which is able to interact with a variety of proteins/peptides. Therefore, the combination of Arg and C17 was chosen as protein binding motifs in this study for proof-of-concept studies in engineering surface chemistry in delivery of different protein payloads. Zwitterionic dendrons with the similar molecular weight with the PEG^{5k} (M_W: 5 kDa) in $PEG^{5k}\text{-}(ArgC17)_4$ were constructed in JDs, denoted as $CB_{16}\text{-}(ArgC17)_4$ and $GPC_8\text{-}(ArgC17)_4$, respectively. ^1H NMR spectra reveal the proportional integrations of protons on C17 and protons to the zwitterionic groups for both $CB_{16}\text{-}(ArgC17)_4$ (Figure 1c) and $GPC_8\text{-}(ArgC17)_4$ (Figure S6), indicating the precise structures as

design. Unfortunately, those JD molecules hard to flight in MALDI-TOF detection due to the entanglements in the self-assemblies. The formula of JD was determined by ^{1}H NMR to be very close to the theoretical ones as shown in Table 1.

Characterization of JD Nanoparticles.

The possession of both protein binding moieties and zwitterionic antifouling functionalities confer JDs with the well-defined and distinct structural and functional disparities. The amphiphilic and protein binding features enable their spontaneous assembly into nanoparticles with protein encapsulated in the core and zwitterionic moieties densely displayed on the surface. The size, morphology, and hydrodynamic diameter of the fabricated zwitterionic nanoparticles were measured using dynamic light scattering (DLS) and transmission electron microscopy (TEM). The results show that both CB_{16}-$(ArgC17)_4$ and GPC_8-$(ArgC17)_4$ form uniform and spherical micelles of 8-9 nm in size (Figure S7 **and** Table 1), which are slightly increased to 11-18 nm after BSA loading (Figure 2 **and** Table 1). The charge relay from the interior guanidine groups to the surface zwitterionic groups in JD causes slightly positive surface charges as indicated by zeta potentials of 13.5 ± 0.9 and 2.4 ± 0.4 mV for CB_{16}-$(ArgC17)_4$ and GPC_8-$(ArgC17)_4$, respectively (Table 1). Upon BSA encapsulation, surface charges were neutralized with zeta potentials decreased to 5.3 ± 0.7 and -3.5 ± 0.3 mV for the CB- and GPC-containing JDs, respectively. The reduction in surface charge suggests the successful inclusion of protein in the nanoparticles. Telodendrimers with PEG chain displayed slightly negative zeta potentials both before and after protein encapsulation,[11] which is correlated with the non-electrolyte feature of PEG. The weakly negative zeta potential of GPC-containing JDs may exhibit better nonfouling and stealth properties than CB nanoparticles.

Evaluation of Protein Binding and Protein Repelling Properties of JD Nanocarrier.

In our previous study,[11] we have estimated the molar ratio of TD to BSA in the nanocomplex equilibrium to be ~9/1 using the isothermal titration calorimetry (ITC) measurements, corresponding to ~1.3/1 in mass ratio. The molar ratio of JD/protein in the complex depends on the size of therapeutic protein, as well as the surface feature of protein. According to the clinical dosage calculation for therapeutic protein administration, mass ratios of protein to TD/JD were provided in the preparation. We applied the agarose gel retention assay to confirm the encapsulation of FITC-BSA by zwitterionic JDs, which prevents protein migration under electrophoresis due to the increased particle size and neutralized surface charge (Figure 3a **and** 3b). Under applied conditions, free FITC-BSA migrated towards anode ascribable to its net negative charges. CB-containing JD was able to suppress FITC-BSA migration, and a continuous shift of BSA migration towards cathode was observed with the increasing CB_{16}-$(ArgC17)_4$ to protein ratio (Figure 3a), which is correlated with the positive surface charges of CB_{16}-$(ArgC17)_4$ (Table 1). Besides, D-CB_{16} dendron slightly slowed BSA migration, indicating the presence of weak interaction owing to the slightly positive charges of CB moieties. By contrast, GPC-containing nanocarriers with an almost neutral surface charge sustained FITC-BSA in the loading wells completely with the increasing JD ratios (Figure 3b). Zwitterionic dendron D-GPC_8 alone exhibited no interference on BSA migration indicating no protein interactions. Interestingly, an on/off status of BSA encapsulation was observed as indicated by the presence of both completely

free FTIC-BSA and fully encapsulated signal at lower GPC_8-$(ArgC17)_4$ to protein ratio of 25/75 w/w. A complete protein loading occurred at a JD to protein ration of 40/60 (w/w) for both polymers. The results imply that the inert surface of GPC-JD nanoparticle coupled with neutral surface charges is preferred for *in vivo* application to reduce protein corona formation.

The encapsulation of protein by JDs was further investigated by establishing a Forster resonance energy transfer (FRET) nanocomplex system using fluorescein-labeled JDs (FITC-CB_{16}-$(ArgC17)_4$ and FITC-GPC_8-$(ArgC17)_4$) and Rhodamin B-labeled BSA (RB-BSA). The fluorescence spectra of RB at the maximum emission of 584 nm were recorded using FITC excitation at 439 nm to indicate the proximity of two molecules for energy transfer. Significant FRET signal was detected when mixing FITC-CB_{16}-$(ArgC17)_4$ and RB-BSA at a ratio of 50/50 (w/w) (Figure 3c), suggesting the encapsulation of RB-BSA by FITC-CB_{16}-$(ArgC17)_4$. The similar phenomena were observed for RB-BSA/FITC-GPC_8-$(ArgC17)_4$ FRET complex. Less than 5% decrease in FRET ratio was observed for both FITC-CB_{16}-$(ArgC17)_4$/RB-BSA and FITC-GPC_8-$(ArgC17)_4$/RB-BSA nanocomplex solutions when 40 mg/mL unlabeled BSA was added (Figure 3d), which indicates the superior stability of the nanocomplex against protein exchanges. In comparison, FITC-PEG^{5k}-$(ArgC17)_4$/RB-BSA nanocomplex with PEG surface was more susceptible to the external protein challenge, resulting in a 14% FRET ratio loss at the serum protein concentration of 40 mg/mL.[11] The results revealed that the zwitterionic surface in JD may be more stable in serum than the PEGylated telodendrimers for protein delivery, due to the enhanced antifouling properties in preventing serum protein adsorption.

The protein adsorption on a nanoparticle surface can be modeled and detected using surface binding techniques via biolayer interferometry (BLI) analysis.[35] Carboxyl-functionalized biosensor tips were activated and reacted with nonfouling materials including PEG^{5k}-NH_2, D-CB_{16}-NH_2, and D-GPC_8-NH_2 with comparable molecular weight (M_W: ~5 kDa), respectively. The modified sensors were then incubated in a BSA solution for protein adsorption study (Figure S8a). Significant protein adsorption was observed on the unmodified biosensor, which was reduced by 30% in magnitude by PEG coating. Impressively, the zwitterionic CB- and GPC-coated surfaces significantly inhibited BSA adsorption. GPC layer completely eliminated protein binding on the biosensor (Figure S8b), indicating the superior antifouling properties.

We further utilized BLI assay to study the protein binding and protein release profiles under serum protein competition as illustrated in Figure 4a. The amine-reactive biosensors were initially coated with BSA via chemical conjugation and then immersed in nanocarrier solutions with varying concentrations for kinetic binding studies, followed by the dissociation process (Figure 4 b-d). Although possessing the identical protein binding dendron, nanocarriers with different antifouling surfaces exhibit different association constants (K_{on}) on BSA-coated sensors as shown in Figure 4e, e.g. 1.32×10^4, 9.55×10^2, and 1.93×10^3 $M^{-1}s^{-1}$ for nanocarriers with PEG, CB, and GPC surfaces, respectively. CB_{16}-$(ArgC17)_4$ and GPC_8-$(ArgC17)_4$ exhibited significant slower association rates, but higher binding magnitudes as compared to PEG^{5k}-$(ArgC17)_4$. The nonspecific interactions of PEG to protein and flexible nature of the PEG chain may contribute to the faster binding rate and

reduced packing density of TDs on the surface. The thicker layer of CB-containing JD on the BLI sensor may be correlated to the slightly higher molecular weight of D-CB$_{16}$ than D-GPC$_8$.

As demonstrated previously,[36] these coating layers on the protein are highly stable in PBS without sufficient dissociation signal observed for a reliable fitting of the dissociation rates. BSA solution at the biological concentration (40 mg/mL) was used to establish a sink condition to compete with nanocarriers binding from the biosensor (Figure 4a). Notably, the significant slower dissociations were observed for nanocarriers with zwitterionic surfaces, as revealed by 20-fold and 10-fold lower apparent dissociation constants (K$_{off}$), for CB$_{16}$-(ArgC17)$_4$ (2.28×10^{-5} s^{-1}) and GPC$_8$-(ArgC17)$_4$ (4.25×10^{-5} s^{-1}) than that of PEG^{5k}-(ArgC17)$_4$ (4.13×10^{-4} s^{-1}). The results indicate that zwitterionic surfaces with the antifouling property efficiently prevent BSA in the solution to adhere onto the nanocomplex surface, thereby reducing protein exchange and preventing premature therapeutic release. The comparable apparent affinity constant (K_D') values were determined to be 31.4, 23.9 and 22.1 nM for nanocarriers with the identical binding partner. However, the drastic difference in dissociation rates (K_{off}') of nanocomplexes in the presence of free BSA emphasizes the importance of the surfaces chemistries on the stability of protein nanocomplex, which is more relevant than K_D' to predict the *in vivo* stability of nanotherapeutics.

JD Nanoparticle Toxicity and Intracellular Protein Delivery.

The *in vitro* cytotoxicity of JDs was tested in cell culture and measured by MTS assay. GPC$_8$-(ArgC17)$_4$ shows nontoxic to SKOV-3 ovarian cancer cells up to 250 μg/mL after 72 h incubation (Figure 5a). Whereas, a dose dependent cytotoxicity was observed for CB$_{16}$-(ArgC17)$_4$ in SKOV-3 cell culture, with only 75% and 30% of cell viability detected at JD concentrations of 50 and 250 μg/mL, respectively (Figure 5a). Such difference in cytotoxicity between GPC-JD and CB-JD were also observed in CHO normal ovary cells and HT29 colon cancer cells (Figure S9). As references, both zwitterionic dendron D-CB$_{16}$-NH$_2$ and D-GPC$_8$-NH$_2$ were also tested and no obvious cytotoxicity were observed at a concentration of 250 μg/mL after 72 h incubation with both SKOV-3 (Figure 5a) and HT29 cancer cells (Figure S9a). Interestingly, normal control cells CHO cell line was observed to be more sensitive to CB dendron D-CB$_{16}$-NH$_2$ similar to CB$_{16}$-(ArgC17)$_4$ with 50% viability lost at 250 μg/mL after 72 h incubation. In contrast, D-GPC$_8$-NH$_2$ dendron is biocompatible for all cells at the tested concentrations (Figure S9b). In addition, JDs and their corresponding zwitterionic dendrons were incubated with red blood cells in the range of 10-500 μg/mL for 24 h. Results in Figure 5b showed that CB$_{16}$-(ArgC17)$_4$ caused ~ 12% hemolysis at a concentration of 500 μg/mL. CB dendron (D-CB$_{16}$-NH$_2$) alone also elicited noticeable dose-dependent hemolysis, which is in agreement with the cytotoxicity measurement at high concentrations. CB moiety possesses a dipole moment of R-⊕-⊖, which is in a direction reverse to the phosphorylcholine (PC) (⊕-⊖-R) on the plasma membrane. Therefore, the charge relay between multiple CB groups with PC on cell membrane (R-⊕-⊖…⊕-⊖-R) may increase membrane activity of CB-based materials, which is similar to the choline phosphate (CP) (R-⊕-⊖) reported in the literature to form dipole-dipole interactions with PC (⊕-⊖-R) on cell membrane.[37] Despite the excellent

hydrophilicity of CB moieties in preventing protein adsorption (Figure 4c), the potential cytotoxicity and hemolytic properties may hinder their *in vivo* applications of the CB-containing JD. In contrast, GPC mimics the component of lipid bilayer plasma membrane, and GPC-JDs were therefore detected to be more biocompatible than CB analogues in both cell viability and hemolytic activity assays.

Many bioactive proteins with poor cell permeability need to be delivered intracellularly to elicit therapeutic activities.[38] Rhodamine B (RB)-labeled BSA was used as a model protein to demonstrate the intracellular protein delivery by JD nanocarriers. As the confocal laser scanning microscopy images revealed in Figure 5c, the cellular uptake of free RB-BSA in SKOV-3 cells was minimal with barely visible fluorescent signal detected. After being loaded into PEGylated arginine-containing PEG^{5k}-$(ArgC17)_4$ nanoparticles, the cell uptake of RB-BSA was increased, which was consistent with our previous observation.[11] For CB_{16}-$(ArgC17)_4$ nanoparticles, relatively weaker RB-BSA signal was observed in the cytoplasm compared with PEGylated nanoparticles, which is likely related to the increased hydrophilicity of the nanoparticle surface. CB moiety bearing a reactive carboxylic acid can be conjugated with targeting ligands to enhance cellular uptake. Therefore, folic acid (FA) was feasibly attached to the surface of CB-containing JD (Figure S10), which significantly improved the cell internalization of RB-BSA. Interestingly, GPC_8-$(ArgC17)_4$ nanocarrier was capable of transporting the loaded protein RB-BSA inside the cells with even higher efficiency under the identical condition. The strong cell uptake of GPC-JD was further confirmed in the repeated experiments for the intracellular delivery of FITC-labeled serum albumin (Figure S11). Additionally, smooth translocation of GPC-JD-RB-BSA from endosome/lysosome into cytoplasm may occur as evidenced by the spread distribution of the delivered protein beyond the endosome/lysosome compartments labeled by green lysotracker (Figure 5c). It indicates the possible additional pathway for cell uptake of GPC-JD nanoparticles in addition to endocytosis. In contrast, RB-BSA in all other nanoformulations including FA-CB-JD was found to co-localize well with the lysotracker.

Endocytosis inhibitors with different inhibitory mechanisms were added into the cell culture medium to explore the pathways involved in the uptake of GPC-containing nanocarrier, including chlorpromazine (10 mg/mL) to inhibit the formation of clathrin vesicles, filipin III (1 mg/mL) for caveolae inhibition, and amiloride (50 mM) as micropinocytosis inhibitor. As shown in the confocal microscopic images (Figure S12), the endocytosis inhibitors only exerted mild inhibitory effects on the cell uptake of RB-BSA loaded in GPC-JD. The result suggests that additional mechanisms, e.g. membrane fusion may contribute, at least partially, to the cell uptake of GPC nanoparticles. As expected, cell culture at low temperature (4 °C) efficiently eliminated the cell uptake of the RB-BSA loaded in GPC nanoparticles (Figure S13), indicating an ATP-dependent and/or thermodynamic processes. GPC-JD exhibited a lower cell uptake in normal cells, e.g. CHO cells, than the SKOV-3 cancer cells for intracellular delivery of RB-BSA, which was at the similar level relative to the PEGylated and CB-containing nanocarriers (Figure S14). Similarly, zwitterionic phosphorylcholine modified gold nanorod,[39] and micellar PC-doxorubicin prodrug[40] were also reported to demonstrate fast, selective, and enhanced uptake within cancer cells as compared to PEGylated counterparts likely through the membrane fusion mechanism bypassing endocytosis. Additionally, RB-BSA loaded in the nanocarriers with PEG, CB and GPC

surface chemistries were observed to have similar yet reduced macrophage uptake in RAW 264.7 cell culture (Figure S15). The presence of active mouse plasma in cell culture (Figure S15a) slightly increased nanoparticle cell uptake than regular culture medium (Figure S15b), due to the surface adsorption of complement proteins in mouse plasma inducing the opsonization of nanoparticles by macrophages.[41, 42] In contrast, free RB-BSA and RB-BSA loaded in FA-CB-JD nanocarrier were observed at higher levels of macrophage uptake (Figure S15) through active mechanisms, e.g. scavenger receptor and folate receptor, respectively. Although the mechanism needs to be further elucidated, the superior cancer cell uptake and endosome escape of the PC-based nanocarrier is highly demanded by the intracellular delivery of therapeutic biomacromolecules.

The enhanced cellular uptake and the subsequent endosomal escape of the payload protein delivered by nanocarrier are critical for the bioactive proteins to target intracellular pathways. In addition, the efficient intracellular protein release is also essential to unleash protein activity. In order to demonstrate the functional intracellular protein delivery by the optimized JD nanocarriers, we select a cytotoxic protein DT_{390} as a payload to be delivered intracellularly to treat cancer cells. Truncated diphtheria toxin (DT_{390}) is a potent protein that induces cell death by inhibiting protein synthesis when translocated into cytoplasm,[43] and therefore was applied as a therapeutic protein to test the efficacy of GPC-JD for intracellular delivery. Free DT_{390} is nontoxic to U87 glioma cells up to a concentration of 12 μg/mL due to its impermeability to the plasma membrane (Figure 5d). DT_{390} encapsulated by nanocarriers induced cell killings in dose-dependent manners for all three formulations. In particular, the potency of DT_{390} delivered by GPC_8-$(ArgC17)_4$ is higher than PEG- and CB-containing nanocarriers with an average 62% of cell elimination after incubation with 12 μg/mL of DT_{390} for 72 h. The cytotoxicity result is consistent with the observation of high accumulation of protein in cell uptake study (Figure 5c). The blank nanocarriers were detected to be nontoxic to U87 cells at the corresponding concentrations used for DT_{390} encapsulation (Figure S16).

Pharmacokinetic (PK) Study of Protein Loaded JD Nanocarriers.

The impact of the surface chemistry of nanoparticles on *in vivo* circulation time was assessed and compared between the zwitterionic GPC-JD and PEG-TD. A small-sized and negatively charged protein α-lactalbumin (α-LA) was labeled with fluorescent dye RB and served as a model protein, which can be efficiently loaded in both telodendrimer PEG^{5k}-$(ArgC17)_4$ (α-LA-PEG-TD) and GPC_8-$(ArgC17)_4$ (α-LA-GPC-JD) nanoparticles as demonstrated by agarose gel electrophoresis (Figure 6a). The protein concentration of free α-LA and α-LA loaded nanoparticles in blood circulation in mice were monitored by measuring the fluorescent intensity of serum after intravenous administration (Figure 6b). Table 2 summarizes the PK parameters obtained by data fitting with a two-compartment model.[44] The blood circulation of α-LA was significantly prolonged by PEGylated telodendrimer nanocarrier, which was further enhanced by the JD NPs with zwitterionic GPC surface. α-LA-GPC-JD displayed the prolonged elimination half-life both at the early distribution phase and the later elimination stage, exhibiting a ~2 folds or > 3 folds increase in half-life compared to PEGylated analogues and free protein, respectively. Accordingly,

the area under the curves (AUC_∞) of a-LA-GPC-JD is 2.2 and 3.4 times higher than α-LA-PEG-TD and the free protein, respectively (Figure 6c **and** Table 2).

Similarly, a fluorescent-labeled synthetic peptide, pH low insertion peptide (pHLIP),[45-47] was able to loaded in our nanocarriers as indicated in agarose gel assay in Figure 6d. Further, the PK profiles of free pHLIP and nanoformulations with PEG and GPC surfaces were recorded in Figure 6e. In a good agreement with the previous study,[45, 46] rapid clearance was observed for free pHLIP exhibiting an elimination time $t_{1/2}$ β of 1.1 h (Table 2). GPC shell increases the half-life of pHLIP by 8 times, which is 3.5-folder longer than that of PEGylated pHLIP. Notably, AUC_∞ of pHLIP in GPC nanoparticle was 3.2-times and 7-times higher than that observed in PEG nanoparticle and free peptide administration, respectively (Figure 6f). The prolonged blood circulations of both pHLIP and a-LA by zwitterionic JD highlight the importance of antifouling GPC chemistry in minimizing protein adsorption, exchange and systemic elimination. The similar uptake of nanoparticles with PEG, CB or JD surface chemistries in normal cells (Figure S14) and macrophage (Figure S15) were observed in the presence of fresh serum plasma during incubation, which was also reported in the literature for nanoparticles with phosphorylcholine surfaces,[40] supporting the prolonged blood circulation of GPC-JD given the improved *in vivo* stability.

In vivo Hypoglycemic Responses by Insulin Treatment.

It is critical to maintain the bioactivity of protein therapeutics after being loaded in the nanoparticles. Insulin was efficiently loaded in JD and TD nanocarriers (Figure 7a) and was subcutaneously injected into the fasted mice to control blood sugar level at a dose of 2 IU/kg. Reduced blood glucose levels were observed in all groups treated with either free insulin or insulin nanoformulations (Figure 7b), indicating the release of the active form of insulin. Free insulin significantly induced the glycemic decrease by 32% after 30 min and the maximal drop occurred after 1 h, followed by a rapid recovery to 80% of a basal level after 2 h. Insulin loaded in PEGylated nanoparticle prolonged the glycemic effects to 1.5-2 h after injection and also followed with a quick recovery, which reached the same level as the free insulin administration at 3 h post-injection. Insulin nanoformulation with GPC surface showed a further delay of hypoglycemic response with the nadir value noted at 2.5 h, and the effect was maintained up to 4 h, indicating the significantly enhanced bioactivity by the controlled release of insulin from GPC-JD nanocarrier. The pharmacological availability (PA) of insulin-GPC-JD was calculated to be 160% in comparison to the free insulin injection, which is also higher than PEGylated nanoformulation with a PA of 120% (Figure 7c).

CONCLUSION

In summary, novel zwitterionic Janus dendrimers were designed and synthesized precisely to achieve efficient protein binding in the core and protein repelling on the surface of nanocarriers. The combinations of solid-phase and liquid-phase peptide syntheses enable the facile introduction of the specific functionalities onto the spatially segregated peripheries of Janus dendrimer. The optimized protein binding partner interacts and encapsulates protein *in situ* driven by the hybrid electrostatic and hydrophobic forces, resulting in the formation of

protein/peptide loaded assemblies. Zwitterionic dendrons are therefore exposed on the surface, rendering the nanoparticle with ultra-low fouling property to resist nonspecific serum protein binding in a biological environment. The optimized zwitterionic JD nanocarrier for protein delivery is characteristic of the favored biocompatibility, enhanced cancer-specific cell uptake, efficient lysosomal escape. The nanocarriers with GPC antifouling surface can greatly prolong the *in vivo* pharmacokinetic profiles of protein relative to the PEGylated nanocarriers, highlighting the desired properties for *in vivo* and intracellular protein therapeutic delivery. The superior property of Janus nanocarrier is also evidenced by the controlled *in vivo* release of insulin and the improved blood sugar control in mice. Given the distinct functionality and freely engineerable framework, such zwitterionic Janus dendrimer has excellent potential to be applied in the fields of *in vivo* therapeutic protein delivery.

EXPERIMENTAL SECTION

Synthesis of Janus Dendrimers by Solid-phase Peptide Synthesis.

Starting from rink amide resin (0.59 mmol/g) Fmoc-Lys (Boc)-OH, PEG-linker-Fmoc, Fmoc-Lys(Fmoc)-OH were coupled sequentially following the standard peptide synthesis procedures. DIC and HOBt were used as coupling reagents. All the coupling reactants were in 3 equivalent molar ratio of the amine functional group on the resin. The completion of the reaction was monitored by the ninhydrin test and confirmed by MALDI-TOF MS of the cleaved compound. Upon completion, residual reactants were removed by filtration under vacuum and washed with copious solvents of DMF, DCM, and MeOH sequentially. Fmoc protecting group was removed by the treatment of resin with 20% 4-methylpiperidine solution in DMF. For the synthesis of CB dendrons, 4-dimethylaminobutyric acid (DMBA) was initially attached at the periphery of oligolysine dendron followed by the reaction with tert-butyl bromoacetate in DMF at 50 °C for 72 h. GPC-COOH synthesized above was directly added to the aminebearing dendron catalyzed by HOBt and DIC. The cleavage of dendrons from rink resin was conducted in TFA/TIS/H$_2$O (95/2.5/2.5, v/v/v) cocktail. Zwitterionic dendrons were purified by precipitation with ethyl ether followed by dialysis against water.

The removal of the Boc protecting group at the focal point of zwitterionic dendrons released primary amine for the initiation of therapeutic-binding dendron synthesis using liquid-phase peptide synthesis following a previously developed procedure.[11] Two consecutive coupling of (Fmoc)-Lys(Fmoc) using HOBt/DIC catalyzed conjugation and Fmoc deprotection steps yielded four branches of primary amine termini. The dendron was then capped with Fmoc-Arg(Pbf)-OH using HOBt/DIC catalyst in DMF. Heptadecanoic acid (C17) was sequentially reacted with the primary amine on arginine peptide and Pbf protecting group was lastly removed in DCM/TFA (50/50, v/v). All products were separated and purified by precipitating in cold ethyl ether for three times.

Bio-layer Interferometry (BLI) Study.

The protein adsorption of zwitterionic dendrimers was investigated by BLI study using BSA as a model protein. The assay was performed on Octet-RED 96 (ForteBio) using 96-well

plate (Greiner Bio-One part no. 655209) at 37 °C. Following the programmed steps, amine reactive biosensors (part no. 18-5029) were hydrated, activated by EDC/sulfo-NHS (20/10 mM) for 300 s, immobilized with polymer (PEG^{5k}-NH$_2$, D-CB$_{16}$-NH$_2$, and D-GPC$_8$-NH$_2$ at 1000 μg/mL, pH 6, respectively) for 800 s, quenched by ethanolamine (pH 8.5) for 400 s, and washed in PBS for 800 s. The protein adsorption was conducted with BSA in PBS at 200 μg/mL for 1000 s followed by dissociation in PBS for 1000 s. All operations were maintained at a 1,000 rpm shaking speed. The real-time chemical immobilizations on the sensor were monitored and the increases of surface thickness were analyzed via Fortebio software.

Protein binding kinetics was conducted using Amine-Reactive Second Generation Dip and Read Biosensors (AR2G, part no. 18-5092). Following defined steps, tips were hydrated and activated for 300 s in EDC/sulfo-NHS solutions (20/10 mM) in H$_2$O. Next, tips were immobilized with BSA at a concentration of 50 μg/mL in acetate buffer (pH 6.0) for 1200 s followed by subsequent quenching for 300 s in a 1 M ethanolamine solution (pH 8.5). The kinetic associations of BSA with polymers were monitored at concentrations of 50, 100, 200, 300, and 400 nM for 2000 s. The dissociation of the polymer was monitored for 2000 s in BSA solution (40 mg/mL in PBS). Baseline-adjusted sensograms were processed by Global fitting to a 1:1 binding model using ForteBio analysis software.

Hemocompatibility Assay.

Fresh blood (1 mL) from healthy human volunteers was collected and diluted into 5 mL of PBS in the presence of 20 mM EDTA. Red blood cells (RBCs) were separated by centrifugation at 3,000 rpm for 10 min. The RBCs were then washed three times with 10 mL of PBS and re-suspended in 20 mL of PBS. Diluted RBC suspension (200 μL) was mixed with zwitterionic dendron or dendrimer solutions at serial concentrations (10, 100, and 500 μg/mL) by gentle vortex and incubated at 37 °C. At determined time, the mixtures were centrifuged at 3,000 rpm for 5 min, and then the hemoglobin in the supernatant was determined by measuring the UV-Vis absorbance at 540 nm (NanoDrop 2000c spectrophotometer, Thermo Scientific). Positive and negative controls were prepared by the incubations of RBCs with Triton-100 (2%) and PBS, respectively. The percent hemolysis of RBCs was calculated using the following formula: RBC hemolysis = [(OD$_{sample}$-OD$_{negative\ control}$)/(OD$_{positive\ control}$-OD$_{negative\ control}$)×100%].

Cell Culture and Cell Viability Assay.

The HT-29 colon and SKOV-3 ovarian cancer cell lines were purchased from American Type Culture Collection (ATCC, Manassas, VA). The human glioblastoma multiforme (GBM) cell line U87 was obtained from the Brain Tumor Laboratory of SUNY Upstate Medical University originally purchased from ATCC (Manassas, VA, USA). The U87 and murine macrophage-like RAW 264.7 cells were cultured in DMEM medium, the Chinese hamster ovary (CHO) cell was grown in RPMI 1640 medium, and HT-29 and SKOV-3 cells were cultured in McCoy's 5A medium, supplemented with 10% fetal bovine serum (FBS), 100 U/mL penicillin G, and 100 mg/mL streptomycin at 37 °C using a humidified 5% CO$_2$ incubator.

The cytotoxicities of unloaded and protein loaded Janus dendrimers were studied by measuring cell viability via MTS assays. Cells were seeded at a cell density of $4 \chi 10^3$ cells per well in 96-well plates. After overnight incubation, the cells were treated with different formulations at serial concentrations. After 72 h incubation, CellTiter 96® aqueous cell proliferation reagent was added to each well according to the manufacturer's instructions. Untreated cells served as negative controls. The cell viability was determined by measuring the absorbance at 490 nm using a microplate reader (BioTek Synergy H1). Results were obtained as the average cell viability of triplicate experiments calculated by a formula of $[(OD_{treat}-OD_{blank})/(OD_{control}-OD_{blank}) \times 100\%]$.

Intracellular Uptake.

The cellular uptake and intracellular trafficking of the protein incorporated JDs were determined by fluorescence microscopy. BSA was used as a model protein, which was chemically labeled with fluorescent dye of RB (RB-BSA) or fluorescein (FITC-BSA). SKOV-3 cells were plated in a well at a density of 5×10^4 cells per well in 300 mL of medium and allowed to adhere for 24 h. The cell was incubated with LysoTracker Green DND-26 for 30 min at 37 °C following the supplier's protocol, and then the RB-BSA or RB-BSA-loaded nanoparticle suspensions (a final BSA concentration at ~60 μg/mL) were added to the culture medium for additional 2 h. Cellular uptakes were terminated by thoughtfully washing cells with PBS for three times and fixed with 4% paraformaldehyde for 15 min at room temperature, and the cell nuclei were stained with 4',6-diamidino-2-phenylindole (DAPI). The slides were mounted with coverslips and cells were visualized and imaged using a laser scanning confocal microscope (Nikon Eclipse T*i*).

The effect of temperature on cell uptake of RB-BSA was studied by the incubation with SKOV-3 cells at 4 °C and 37 °C for 2 h. The cells were imaged under fluorescence microscope (Leica DMI3000B, Heidelberg, Germany). To study the effects of different endocytosis inhibitors on the cellular uptake of nanocarriers, SKOV-3 cells were pre-incubated for 1 h at 37 °C with the following three inhibitors: chlorpromazine (CPZ, 10 mg/mL) to inhibit the formation of clathrin vesicles, filipin III (1 mg/mL) for caveolae inhibition, and amiloride (50 mM) as micropinocytosis inhibitor. RB-BSA loaded GPC_8-$(ArgC17)_4$ nanocarrier was added to the medium containing the indicated inhibitors and incubated with SKOV-3 cell for additional 2 h at 37 °C. The cells were then washed, fixed and nuclei stained as described above.

Animals.

BALB/c mice, at age 6-7 weeks, were purchased from Charles River Laboratories (Wilmington, MA). All animals were kept under pathogen-free conditions according to Association for Assessment and Accreditation of Laboratory Animal Care (AAALAC) guidelines and were allowed to acclimatize for at least 4 days prior to any experiments. All animal experiments were performed in compliance with institutional guidelines and according to protocol approved by the Committee for the Humane Use of Animals of State University of New York Upstate Medical University.

Pharmocokinetic (PK) Study.

The blood circulations of biomacromolecules were studied using different model compounds including peptide and protein. The PKs of native and polymer encapsulated α-Lactalbumin (α-LA, M_W: 14 kDa) and pH low insertion peptide (pHLIP, M_W: ~6 kDa) [45-47] were studied on BALB/c mice (n=3 per group). Rhodamine B-labeled α-LA (RB-α-LA) and pHLIP were intravenously injected at a dose of 8 mg/kg and 1 mg/kg, respectively. At pre-determined time after injection, blood samples were collected in heparinized vials from the tail vein, and plasma was separated by centrifugation for quantitative measurement. The fluorescent signal of RB-α-LA was recorded at excitation/emission of 525/580 nm on a fluorescence microplate reader Synergy H1 (BioTek Instruments Inc., Winooski, VT) and pHLIP was collected at excitation/emission of 630/671 nm on SpectraMax i3 plate reader (Molecular Devices, Sunnyvale, CA).

Hypoglycemic Effect of Insulin.

The hypoglycemic effects of the insulin (M_W: 5807 Da) and insulin nanoformulations following subcutaneous administration were evaluated on healthy BALB/c mice (n= 6 per group) at insulin dose of 2IU/kg. The mice were fasted for overnight before the injection with only water access and stay fasted during the test. The insulin loaded nanoparticles were produced at a mass ratio of 1/10 of insulin to polymer. Blood glucose levels were measured using a glucose meter (EasyTouch®, MHC Medical Products, LLC, Fairfield, OH). The areas above the curves (AAC) of the concentration-time profiles were calculated with the trapezoidal method. The AAC was used to calculate the relative pharmacological bioavailability (PA) following the following equation, PA %=(AAC$_{NPs}$/Does$_{NPs}$)/(AAC$_{ins}$/Does$_{ins}$)× 100%

Statistical Analysis.

Data are presented as means ± standard deviation (SD). All statistical analyses were performed using Student's t-test for comparison of two groups. The level of statistical significance was set with $P < 0.05$ considered significant. The half maximal inhibitory concentration (IC$_{50}$) values were calculated from cell viability curves by fitting a dose–response model using sigmoidal function with variable Hillslope. Pharmacokinetic data were fitted to a two-compartment model.

Supplementary Material

Refer to Web version on PubMed Central for supplementary material.

ACKNOWLEDGMENTS

REFERENCES

[1]. Mitragotri S, Burke PA, Langer R, Overcoming the challenges in administering biopharmaceuticals: formulation and delivery strategies, Nature reviews Drug discovery 13(9) (2014)655–672. [PubMed: 25103255]

[2]. Chang H, Zhang J, Wang H, Lv J, Cheng Y, A Combination of Guanidyl and Phenyl Groups on a Dendrimer Enables Efficient siRNA and DNA Delivery, Biomacromolecules 18(8) (2017) 2371–2378. [PubMed: 28686016]

[3]. Chang H, Lv J, Gao X, Wang X, Wang H, Chen H, He X, Li L, Cheng Y, Rational Design of a Polymer with Robust Efficacy for Intracellular Protein and Peptide Delivery, Nano letters 17(3) (2017) 1678–1684. [PubMed: 28206763]

[4]. Bayele HK, Ramaswamy C, Wilderspin AF, Srai KS, Toth I, Florence AT, Protein transduction by lipidic peptide dendrimers, J Pharm Sci 95(6) (2006) 1227–37. [PubMed: 16639724]

[5]. Gu Z, Biswas A, Zhao M, Tang Y, Tailoring nanocarriers for intracellular protein delivery, Chem Soc Rev 40(7) (2011) 3638–55. [PubMed: 21566806]

[6]. Yu M, Wu J, Shi J, Farokhzad OC, Nanotechnology for protein delivery: Overview and perspectives, J Control Release 240 (2016) 24–37. [PubMed: 26458789]

[7]. Kojima C, Kameyama R, Yamada M, Ichikawa M, Waku T, Handa A, Tanaka N, Ovalbumin delivery by guanidine-terminated dendrimers bearing an amyloid-promoting peptide via nanoparticle formulation, Bioconjugate chemistry 26(8) (2015) 1804–1810. [PubMed: 26186179]

[8]. Lv J, He B, Yu J, Wang Y, Wang C, Zhang S, Wang H, Hu J, Zhang Q, Cheng Y, Fluoropolymers for intracellular and in vivo protein delivery, Biomaterials 182 (2018) 167–175. [PubMed: 30121426]

[9]. Zhang Z, Shen W, Ling J, Yan Y, Hu J, Cheng Y, The fluorination effect of fluoroamphiphiles in cytosolic protein delivery, Nature communications 9(1) (2018) 1377.

[10]. Yu C, Tan E, Xu Y, Lv J, Cheng Y, A Guanidinium-Rich Polymer for Efficient Cytosolic Delivery of Native Proteins, Bioconjugate chemistry 30(2) (2018) 413–417. [PubMed: 30383369]

[11]. Wang X, Shi C, Zhang L, Bodman A, Guo D, Wang L, Hall WA, Wilkens S, Luo J, Affinity-controlled protein encapsulation into sub-30 nm telodendrimer nanocarriers by multivalent and synergistic interactions, Biomaterials 101 (2016) 258–271. [PubMed: 27294543]

[12]. Wang X, Shi C, Zhang L, Lin MY, Guo D, Wang L, Yang Y, Duncan TM, Luo J, Structure-Based Nanocarrier Design for Protein Delivery, ACS Macro Letters (2017) 267–271.

[13]. Albanese A, Tang PS, Chan WC, The effect of nanoparticle size, shape, and surface chemistry on biological systems, Annual review of biomedical engineering 14 (2012) 1–16.

[14]. Walkey CD, Olsen JB, Guo H, Emili A, Chan WCW, Nanoparticle Size and Surface Chemistry Determine Serum Protein Adsorption and Macrophage Uptake, Journal of the American Chemical Society 134(4) (2012) 2139–2147. [PubMed: 22191645]

[15]. Monopoli MP, Åberg C, Salvati A, Dawson KA, Biomolecular coronas provide the biological identity of nanosized materials, Nature nanotechnology 7(12) (2012) 779.

[16]. Halperin A, Polymer Brushes that Resist Adsorption of Model Proteins: Design Parameters, Langmuir 15(7) (1999) 2525–2533.

[17]. Wu J, Zhao C, Lin W, Hu R, Wang Q, Chen H, Li L, Chen S, Zheng J, Binding characteristics between polyethylene glycol (PEG) and proteins in aqueous solution, Journal of Materials Chemistry B 2(20) (2014) 2983–2992.

[18]. Chen S, Li L, Zhao C, Zheng J, Surface hydration: Principles and applications toward low-fouling/nonfouling biomaterials, Polymer 51(23) (2010) 5283–5293.

[19]. Settanni G, Zhou J, Suo T, Schottler S, Landfester K, Schmid F, Mailander V, Protein corona composition of poly(ethylene glycol)- and poly(phosphoester)-coated nanoparticles correlates strongly with the amino acid composition of the protein surface, Nanoscale 9(6) (2017) 2138–2144. [PubMed: 28124700]

[20]. Pelaz B, del Pino P, Maffre P, Hartmann R, Gallego M, Rivera-Fernández S, de la Fuente JM, Nienhaus GU, Parak WJ, Surface Functionalization of Nanoparticles with Polyethylene Glycol: Effects on Protein Adsorption and Cellular Uptake, ACS Nano 9(7) (2015) 6996–7008. [PubMed: 26079146]

[21]. Bertrand N, Grenier P, Mahmoudi M, Lima EM, Appel EA, Dormont F, Lim JM, Karnik R, Langer R, Farokhzad OC, Mechanistic understanding of in vivo protein corona formation on polymeric nanoparticles and impact on pharmacokinetics, Nature communications 8(1) (2017) 777.

[22]. Jiang S, Cao Z, Ultralow-fouling, functionalizable, and hydrolyzable zwitterionic materials and their derivatives for biological applications, Advanced Materials 22(9) (2010) 920–932. [PubMed: 20217815]

[23]. Zhang P, Sun F, Tsao C, Liu S, Jain P, Sinclair A, Hung H-C, Bai T, Wu K, Jiang S, Zwitterionic gel encapsulation promotes protein stability, enhances pharmacokinetics, and reduces immunogenicity, Proceedings of the National Academy of Sciences 112(39) (2015) 12046–12051.

[24]. Liang S, Liu Y, Jin X, Liu G, Wen J, Zhang L, Li J, Yuan X, Chen IS, Chen W, Phosphorylcholine polymer nanocapsules prolong the circulation time and reduce the immunogenicity of therapeutic proteins, Nano Research 9(4) (2016) 1022–1031.

[25]. Lowe AB, McCormick CL, Synthesis and solution properties of zwitterionic polymers, Chem Rev 102(11) (2002) 4177–89. [PubMed: 12428987]

[26]. Zhang S, Sun HJ, Hughes AD, Moussodia RO, Bertin A, Chen Y, Pochan DJ, Heiney PA, Klein ML, Percec V, Self-assembly of amphiphilic Janus dendrimers into uniform onion-like dendrimersomes with predictable size and number of bilayers, Proc Natl Acad Sci U S A 111(25) (2014) 9058–63. [PubMed: 24927561]

[27]. Percec V, Wilson DA, Leowanawat P, Wilson CJ, Hughes AD, Kaucher MS, Hammer DA, Levine DH, Kim AJ, Bates FS, Davis KP, Lodge TP, Klein ML, DeVane RH, Aqad E, Rosen BM, Argintaru AO, Sienkowska MJ, Rissanen K, Nummelin S, Ropponen J, Self-assembly of Janus dendrimers into uniform dendrimersomes and other complex architectures, Science 328(5981) (2010) 1009–14. [PubMed: 20489021]

[28]. Dong Y, Yu T, Ding L, Laurini E, Huang Y, Zhang M, Weng Y, Lin S, Chen P, Marson D, Jiang Y, Giorgio S, Pricl S, Liu X, Rocchi P, Peng L, A Dual Targeting Dendrimer-Mediated siRNA Delivery System for Effective Gene Silencing in Cancer Therapy, J Am Chem Soc 140(47) (2018) 16264–16274. [PubMed: 30346764]

[29]. Nummelin S, Liljestrom V, Saarikoski E, Ropponen J, Nykanen A, Linko V, Seppala J, Hirvonen J, Ikkala O, Bimbo LM, Kostiainen MA, Self-assembly of amphiphilic Janus dendrimers into mechanically robust supramolecular hydrogels for sustained drug release, Chemistry 21(41) (2015) 14433–9. [PubMed: 26134175]

[30]. Wang X, Shi C, Zhang L, Lin MY, Guo D, Wang L, Yang Y, Duncan TM, Luo J, Structure-Based Nanocarrier Design for Protein Delivery, ACS Macro Letters 6(3) (2017) 267–271.

[31]. Carr LR, Xue H, Jiang S, Functionalizable and nonfouling zwitterionic carboxybetaine hydrogels with a carboxybetaine dimethacrylate crosslinker, Biomaterials 32(4) (2011) 961–968. [PubMed: 20970184]

[32]. Laschewsky A, Zerbe I, Polymerizable and polymeric zwitterionic surfactants: 1. Synthesis and bulk properties, Polymer 32(11) (1991) 2070–2080.

[33]. Ishihara K, Mu M, Konno T, Inoue Y, Fukazawa K, The unique hydration state of poly(2-methacryloyloxyethyl phosphorylcholine), J Biomater Sci Polym Ed 28(10-12) (2017) 884–899. [PubMed: 28276997]

[34]. Guo D, Shi C, Wang X, Wang L, Zhang S, Luo J, Riboflavin-containing telodendrimer nanocarriers for efficient doxorubicin delivery: High loading capacity, increased stability, and improved anticancer efficacy, Biomaterials (2017).

[35]. Ramadan MH, Prata JE, Karácsony O, Dunér G, Washburn NR, Reducing Protein Adsorption with Polymer-Grafted Hyaluronic Acid Coatings, Langmuir 30(25) (2014) 7485–7495. [PubMed: 24892924]

[36]. Wang X, Bodman A, Shi C, Guo D, Wang L, Luo J, Hall WA, Tunable Lipidoid - Telodendrimer Hybrid Nanoparticles for Intracellular Protein Delivery in Brain Tumor Treatment, Small 12(31) (2016) 4185–4192. [PubMed: 27375237]

[37]. Yu X, Liu Z, Janzen J, Chafeeva I, Horte S, Chen W, Kainthan RK, Kizhakkedathu JN, Brooks DE, Polyvalent choline phosphate as a universal biomembrane adhesive, Nature materials 11(5) (2012) 468. [PubMed: 22426460]

[38]. Yu M, Wu J, Shi J, Farokhzad OC, Nanotechnology for protein delivery: Overview and perspectives, Journal of Controlled Release 240 (2016) 24–37. [PubMed: 26458789]

[39]. Zhou W, Shao J, Jin Q, Wei Q, Tang J, Ji J, Zwitterionic phosphorylcholine as a better ligand for gold nanorods cell uptake and selective photothermal ablation of cancer cells, Chemical Communications 46(9) (2010) 1479–1481. [PubMed: 20162154]

[40]. Wang H, Liu X, Wang Y, Chen Y, Jin Q, Ji J, Doxorubicin conjugated phospholipid prodrugs as smart nanomedicine platforms for cancer therapy, Journal of Materials Chemistry B 3(16) (2015) 3297–3305.

[41]. Owens DE III, Peppas NA, Opsonization, biodistribution, and pharmacokinetics of polymeric nanoparticles, International journal of pharmaceutics 307(1) (2006) 93–102. [PubMed: 16303268]

[42]. Xiao K, Li Y, Luo J, Lee JS, Xiao W, Gonik AM, Agarwal RG, Lam KS, The effect of surface charge on in vivo biodistribution of PEG-oligocholic acid based micellar nanoparticles, Biomaterials 32(13) (2011) 3435–3446. [PubMed: 21295849]

[43]. Schmohl JU, Todhunter D, Oh S, Vallera DA, Mutagenic Deimmunization of Diphtheria Toxin for Use in Biologic Drug Development, Toxins 7(10) (2015) 4067–4082. [PubMed: 26473923]

[44]. Zhang Y, Huo M, Zhou J, Xie S, PKSolver: An add-in program for pharmacokinetic and pharmacodynamic data analysis in Microsoft Excel, Computer methods and programs in biomedicine 99(3) (2010) 306–314. [PubMed: 20176408]

[45]. Vᵉvere AL, Biddlecombe GB, Spees WM, Garbow JR, Wijesinghe D, Andreev OA, Engelman DM, Reshetnyak YK, Lewis JS, A novel technology for the imaging of acidic prostate tumors by positron emission tomography, Cancer research 69(10) (2009) 4510–4516. [PubMed: 19417132]

[46]. Reshetnyak YK, Yao L, Zheng S, Kuznetsov S, Engelman DM, Andreev OA, Measuring tumor aggressiveness and targeting metastatic lesions with fluorescent pHLIP, Molecular Imaging and Biology 13(6) (2011) 1146–1156. [PubMed: 21181501]

[47]. Demoin DW, Wyatt LC, Edwards KJ, Abdel-Atti D, Sarparanta M, Pourat J, Longo VA, Carlin SD, Engelman DM, Andreev OA, Reshetnyak YK, Viola-Villegas N, Lewis JS, PET Imaging of Extracellular pH in Tumors with 64Cu- and 18F-Labeled pHLIP Peptides: A Structure-Activity Optimization Study, Bioconjugate Chemistry 27(9) (2016) 2014–2023. [PubMed: 27396694]
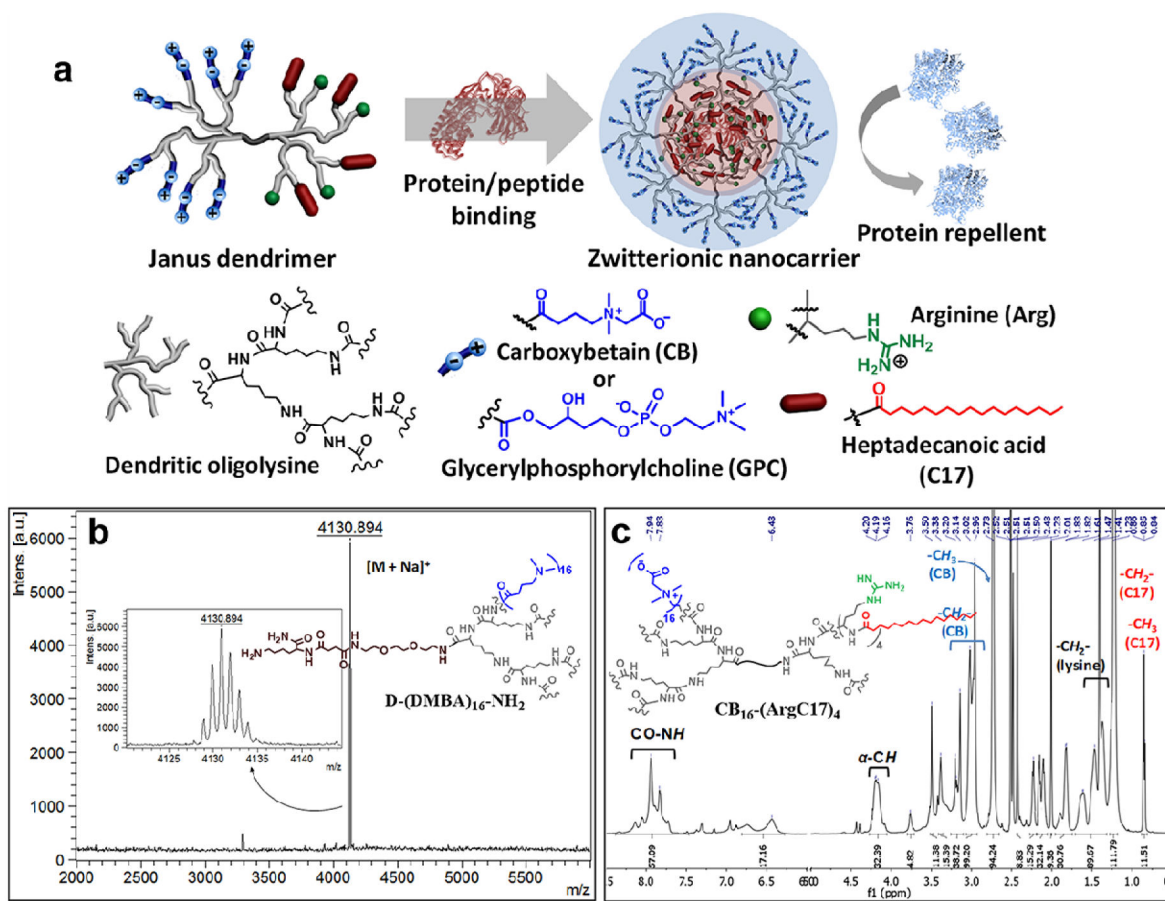
Figure 1.
a) Schematic representation of the chemical structure of zwitterionic Janus dendrimer with the protein binding and antifouling features. b) MALDI-TOF MS spectrum of precursor dendron D-(DMBA)$_{16}$-NH$_2$ synthesized by solid-phase peptide approach. c) Representative ^{1}H NMR spectrum of Janus dendrimer CB$_{16}$-(ArgC17)$_4$ (calculated as CB$_{15.9}$-(ArgC17)$_{3.8}$).
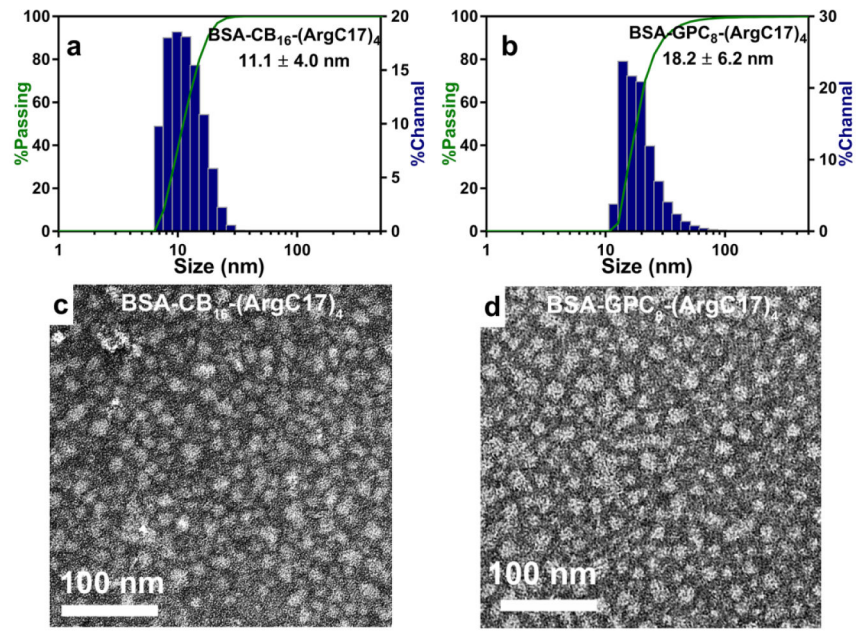
Figure 2.
Characterization of particle sizes and morphologies of BSA loaded JDs. Hydrodynamic sizes (a and b) and TEM images (c and d) of BSA loaded CB_{16}-$(ArgC17)_4$ and GPC_8-$(ArgC17)_4$ nanoparticles.
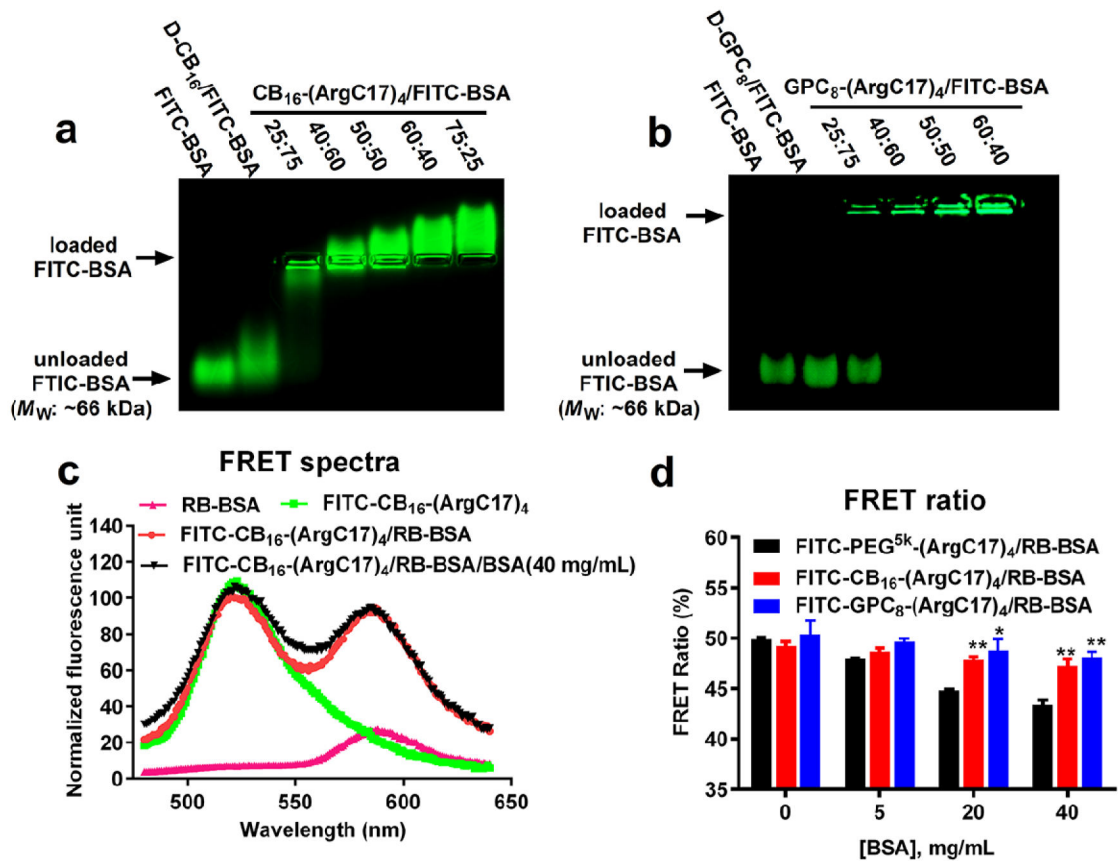
Figure 3.
Protein loading studies of JDs using BSA as a model protein. Agarose gel electrophoresis profiles showing the encapsulation efficiency of FITC-BSA by (a) CB_{16}-$(ArgC17)_4$ and (b) GPC_8-$(ArgC17)_4$. D-CB_{16} and D-GPC_8 represent the corresponding zwitterionic dendrons. (c) Representative fluorescence emission spectra of RB-BSA, FITC-CB_{16}-$(ArgC17)_4$ and the FRET nanocomplex of both (50/50, w/w) excited at FITC channel $\lambda ex = 439$ nm) in the absence and presence of 40 mg/mL of external BSA. The fluorescence spectrum was normalized by the intensity at 528 nm. (d) FRET ratios of FITC-PEG^{5k}-$(ArgC17)_4$, FITC-CB_{16}-$(ArgC17)_4$, and FITC-GPC_8-$(ArgC17)_4$ with RB-BSA (50/50, w/w) after incubation with BSA solutions at different concentrations (*P < 0.05, **P < 0.01 when compared with FITC-PEG^{5k}-$(ArgC17)_4$/RB-BSA group).
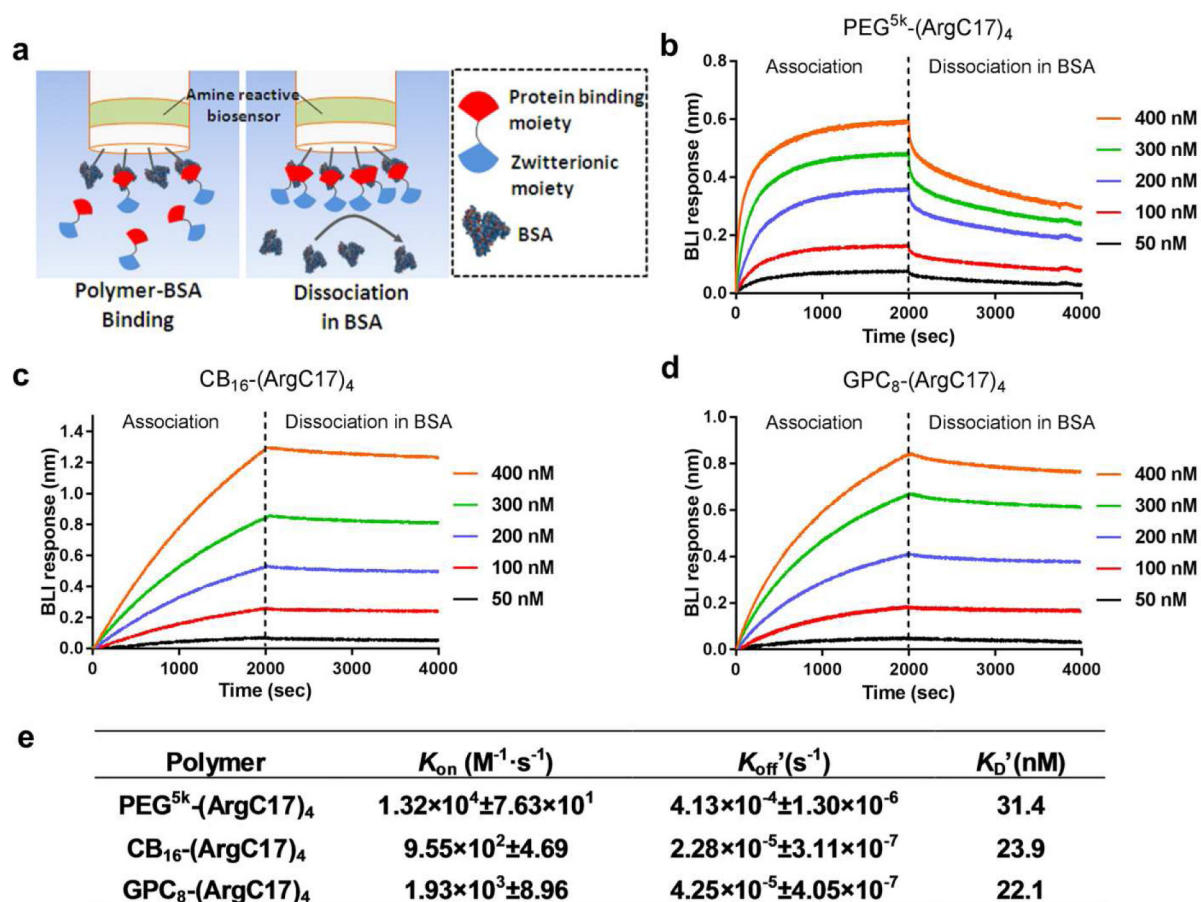
Figure 4.
(a) Schematic illustration of the association in protein binding polymer solution (left) and dissociation in BSA solution (right) for the amine reactive biosensors immobilized with BSA. BLI kinetics assays for association in (b) PEG^{5k}-$(ArgC17)_4$, (c) CB_{16}-$(ArgC17)_4$, and (d) GPC_8-$(ArgC17)_4$ solutions in the concentration range of 50-400 nM and dissociation in BSA solutions (40 mg/mL). (e) Summary of BLI kinetic parameters from the kinetic assay (b-d).
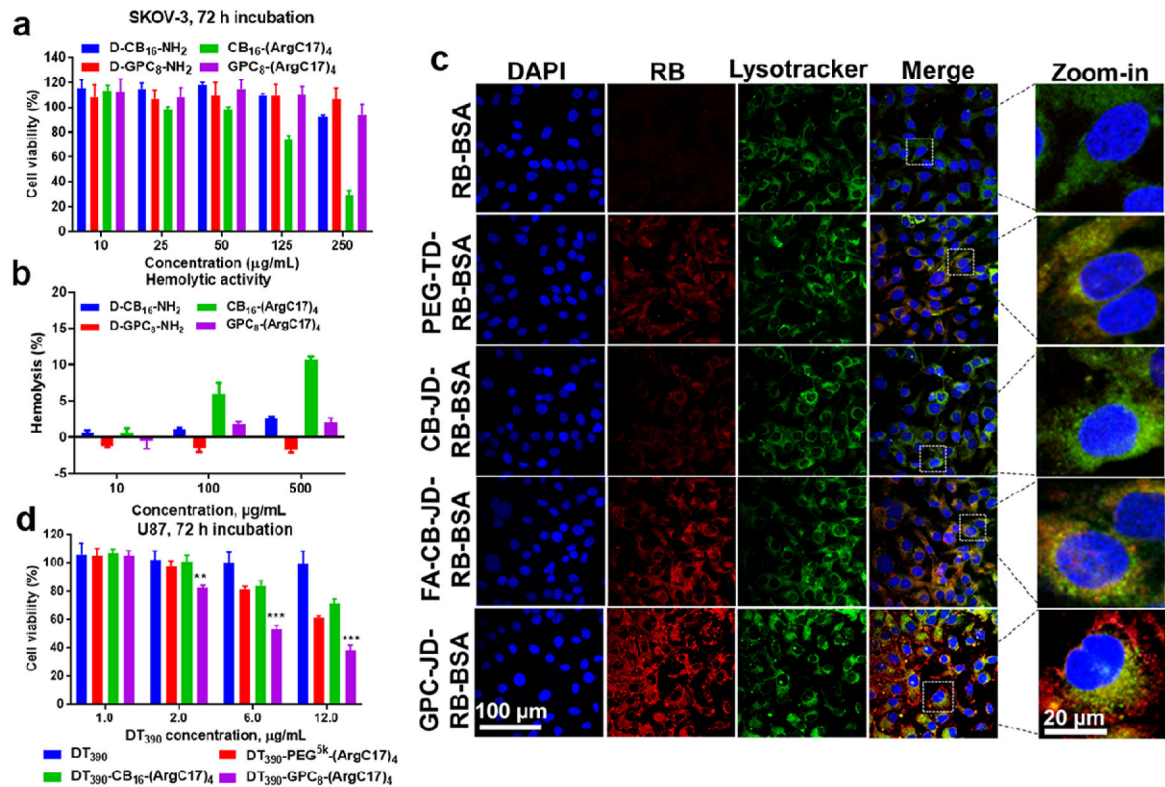
Figure 5.
In vitro biocompatibility and cellular uptake of zwitterionic dendrons and JDs. (a) Cell viability of SKOV-3 cell after 72 h incubation with the indicated materials as measured by MTS assay. (b) Hemolytic activities of zwitterionic materials towards red blood cells after 24 h incubation at different concentrations. (c) Confocal images showed the intracellular trafficking of rhodamin B-labeled BSA (RB-BSA) and RB-BSA loaded nanocarriers by SKOV-3 cells. PEGylated telodendrimer, PEG^{5k}-$(ArgC17)_4$ was applied to encapsulate RB-BSA, in comparison to Janus nanocarriers of CB_{16}-$(ArgC17)_4$ (CB-JD), FA-CB_{16}-$(ArgC17)_4$ (FA-CB-JD), and GPC_8-$(ArgC17)_4$ (GPC-JD). (d) Cell killing assay in U87 glioma cell culture for DT_{390} and DT_{390} loaded in nanocarriers with the mass ratio of 1/3 (DT_{390}/TD or JDs). (**$P < 0.01$, ***$P < 0.001$ when comparing DT_{390}-GPC_8-$(ArgC17)_4$ with other groups).
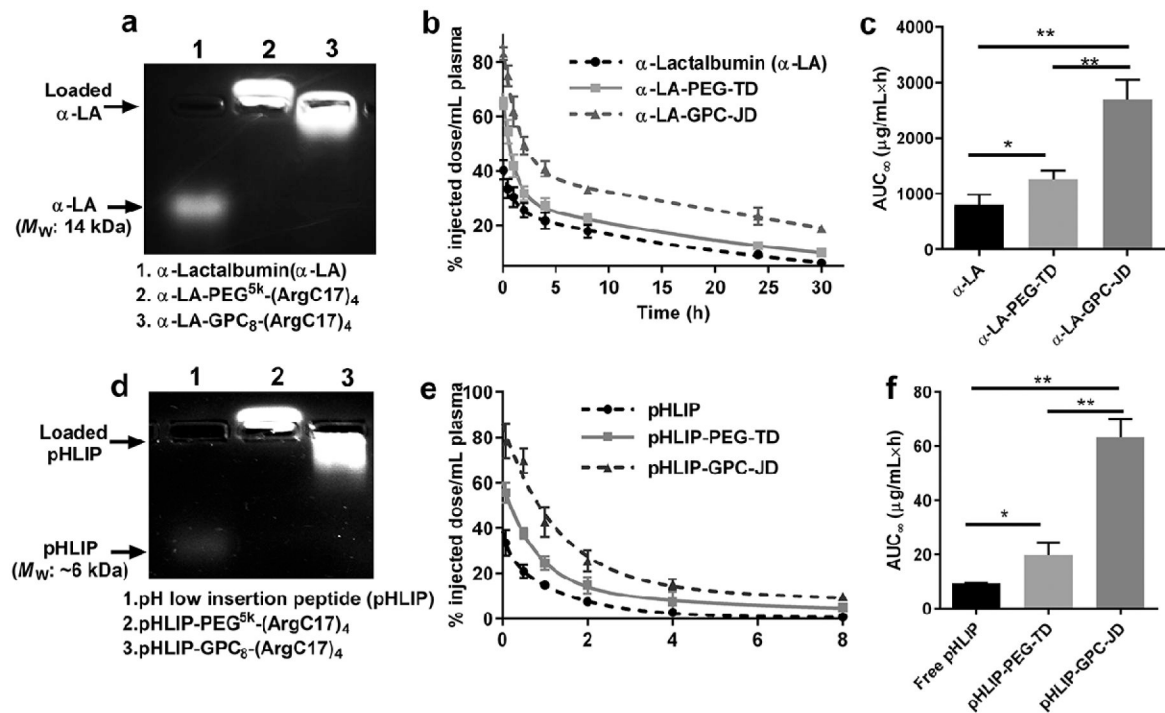
Figure 6.
Pharmacokinetic studies of α-LA and pHLIP. (a) Agarose gel electrophoresis profile showing the loading of α-LA in JD or TD nanocarrier with the mass ratio of 1/5 (α- LA/JD or α-LA/TD). (b) Blood circulation profiles and (c) area under curves for α-LA and α-LA loaded nanoparticles following intravenous administration. (d) Agarose gel electrophoresis profile of pHLIP loading in JD or TD nanocarrier with the mass ratio of 1/8 (pHLIP/JD or pHLIP/TD). (e) Blood circulation profiles and f) area under curves for native pHLIP and pHLIP loaded nanoparticles. (*P < 0.05, **P < 0.01).
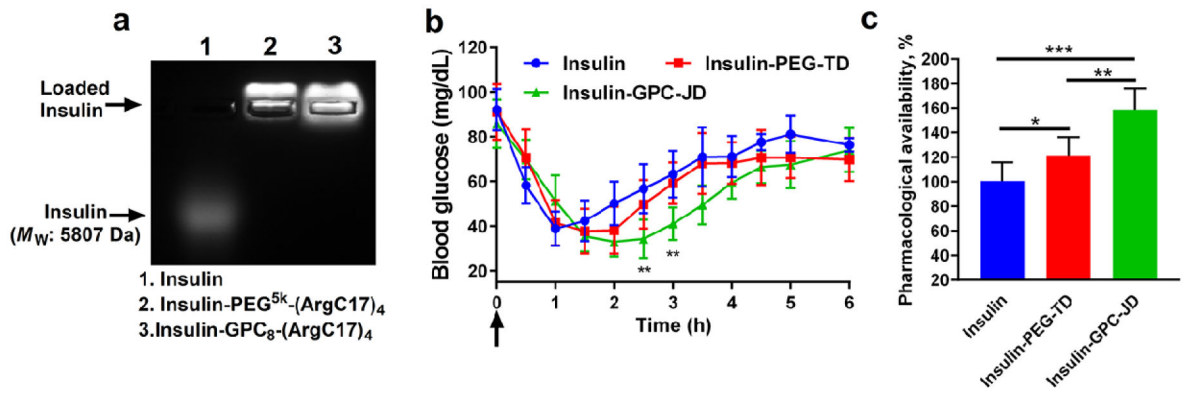
Figure 7.
(a) Agarose gel electrophoresis profile of insulin encapsulation in TD and JD nanocarriers with the mass ratio of 1/10 (insulin/JD or insulin/TD). (b) Blood glucose response of normal mice after subcutaneous injection with free insulin or insulin-loaded nanoparticles at insulin dose of 2 IU/kg (n=6, **P < 0.01 for treatments between Insulin-GPC-JD and Insulin-PEG-TD). (c) The pharmacological availability of insulin formulations in blood sugar control profiles (0-6 h). (*P < 0.05, **P < 0.01, ***P < 0.001).

Table 1.

Physicochemical properties of zwitterionic dendrimers.

Janus Dendrimers	Formula by NMR	CMC^a (μg/mL)	D_h^b (nm)	ζ^c (mV)	D_h with BSA^d (nm)	ζ with BSA^e (mV)
CB_{16}-$(ArgC17)_4$	$CB_{15.9}$-$(ArgC17)_{3.8}$	9.6	8.3 ± 2.0	13.5 ± 0.9	11.1 ± 4.0	5.3 ± 0.7
GPC_8-$(ArgC17)_4$	$GPC_{8.1}$-$(ArgC17)_{3.8}$	11.8	9.3 ± 2.5	2.4 ± 0.4	18.2 ± 6.2	−3.5 ± 0.3
PEG^{5k}-$(ArgC17)_4{}^f$	PEG^{5k}-$(ArgC17)_{3.8}$	2.7	11 ± 3	−4.6 ± 0.7	10 ± 4	−5.1 ± 0.7

[a] Measured by fluorescent method using Nile red dye as a probe.

[b] Hydrodynamic size measured by DLS analysis at a JD concentration of 5 mg/mL. Data was expressed as mean ± SD, where SD is the half width at maximum height.

[c] Zeta potential measured at a concentration of 1 mg/mL. Data was expressed as mean ± standard deviation.

[d] Measured at a JD concentration of 5 mg/mL with a JD/BSA ratio of 60/40 (w/w).

[e] Obtained at a JD concentration of 1 mg/mL with a JD/BSA ratio of 60/40 (w/w).

[f] Data can be found in [11].

Table 2.

Pharmacokinetic parameters of α-LA and peptide after intravenous injections.

PK parameter	α-LA			pHLIP		
	Native α-LA	α-LA-PEG-TD	α-LA-GPC-JD	pHLIP	pHLIP-PEG-TD	pHLIP-GPC-JD
$t_{1/2}$ α (h)[a]	0.025±0.002	0.31±0.19	0.74±0.16	0.022±0.002	0.048±0.007	0.93±0.27
$t_{1/2}$ β (h)[b]	10.3±2.4	15.3±4.0	30.9±4.4	1.2±0.2	2.8±1.4	9.9±2.9
CL (mL/h)[c]	21.1±1.8	3.2±2.5	0.72±0.22	20.1±3.3	7.2±0.7	0.37±0.20
AUC_∞ (μg/mL×h)[d]	805.9±179.6	1253.5±161.2	2762.2±291.8	9.4±0.3	19.8±4.7	63.5±6.7

[a]Initial half-life.

[b]Terminal elimination half-life.

[c]Apparent total clearance of the protein from plasma.

[d]Area under the curve from time zero to infinity.